Analysis of the $5p^6 \rightarrow 5p^5nl$ $(J=1)$ Rydberg series in Ba^{2+}

W. T. Hill, III
University of Maryland, College Park, Maryland 20742

J. Sugar and T. B. Lucatorto
National Bureau of Standards, Gaithersburg, Maryland 20899

K. T. Cheng
Lawrence Livermore National Laboratory, Livermore, California 94550

(Received 25 March 1987)

A detailed analysis is made for the bound $5p^6 \rightarrow 5p^5ns,nd$ levels observed in the photoabsorption of Ba^{2+}. A multichannel quantum-defect theory approach, with *ab initio* calculations for some of the parameters, is used to describe periodic enhancements in intensity associated with interchannel mixing. Qualitative agreement between experiment and theory requires the inclusion of plasma-broadening effects to account for the apparent increase in strength of the higher n levels.

I. INTRODUCTION

In an earlier paper[1] we gave an interpretation of our $5p^6 \rightarrow 5p^5ns,nd$ observations of Ba^{2+} between the $5p^5\,{}^2P_{3/2}$ (I_1) and $^2P_{1/2}$ (I_2) thresholds. The spectrum showed the dramatic effects of the increasing nuclear charge along the Xe I isoelectronic sequence. These are manifested in the sharpening of the autoionizing resonances as channel mixing decreases with increasing central potential and in the bunching of eigenquantum-defect values as the Lu-Fano plot[2] approaches the limit of three horizontal and two vertical lines with very sharp avoided crossings. We showed that strong-term dependence in the beginning of the isoelectronic sequence reflects large correlation effects which gradually diminish as one proceeds to higher-charged ions. The detailed analysis of the spectrum below the I_1 threshold (see Fig. 1), largely ignored in the first paper, will be the subject of the present work.

Our presentation is based on a multichannel quantum-defect theory (MQDT) approach[2] utilizing the effective quantum numbers denoted ν_1 and ν_2 defined by the relationships

$$\frac{Z_c^2}{\nu_i^2} = I_i - E, \quad i = 1,2$$

where E is the energy of the atomic level (expressed in Rydbergs as are I_1 and I_2) and Z_c $(=3$ for $Ba^{2+})$ is the residual core charge. The results of a relativistic random-phase approximation (RRPA) calculation (cf. Ref. 3), adjusted by comparison with the observed spectrum, provide the MQDT parameters which enable us to draw the detailed Lu-Fano plot in each period through to the continuum and to explain qualitatively the spectral intensity variations.

II. EXPERIMENTAL PROCEDURE

In general, high-lying bound and autoionizing Rydberg states can best be observed by absorption spectroscopy.

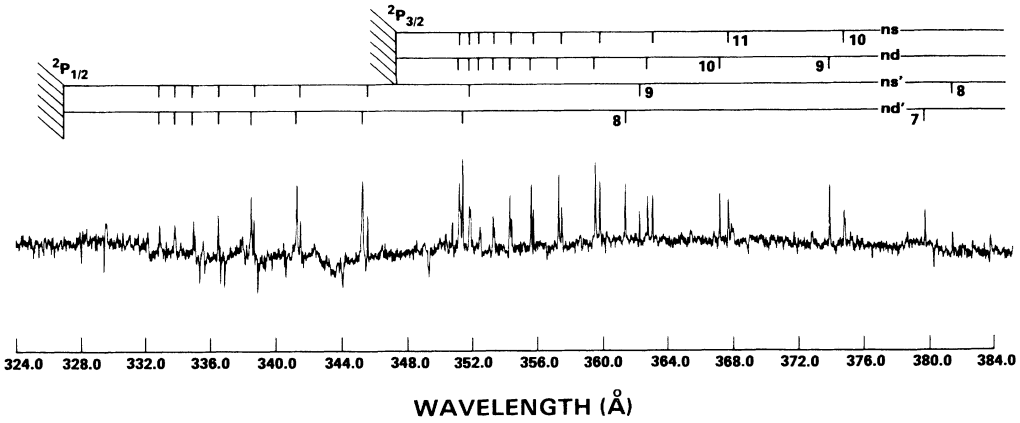

FIG. 1. Normalized densitometer trace of photographic absorption spectrum plotted as a function of wavelength. Level assignments and series limit are indicated by bar graph above spectrum.

To produce a sufficient density of Ba^{2+} ions we used the resonant laser-driven ionization technique[4] applied in two stages: the first to convert the Ba vapor in a heat pipe to a Ba^+ plasma and the second to ionize the Ba^+ into a Ba^{2+} plasma.

The apparatus is shown in Fig. 2. Ba vapor at a pressure of 0.5 torr, confined to a 10 cm length by the buffer gas (He) was contained in a heat-pipe oven (temperature at 1200 K). The first laser was tuned to the $6s^2\,{}^1S_0 \rightarrow 6s6p\,{}^1P_1$ neutral Ba transition (5535 Å) and ionized nearly 100% of the Ba along the line of sight. A second laser fired $\sim 1\ \mu$s later was tuned to the $6s^2S_{1/2} \rightarrow 6p\,{}^2P_{1/2}$ transition in Ba^+ (4935 Å) and generated the desired Ba^{2+}. A Ba^{2+} density of $\sim 10^{16}$ cm^{-3} could be achieved when the bandwidth and energies of the lasers were about 1 Å and 1 MW/cm^2, respectively. A pulsed Ballofet-Romand-Vodar (BRV) high-voltage spark continuum light source was triggered[5] about 1 μs after the second laser to produce the absorption spectra of Ba^{2+}. This source was run with a uranium anode which gave an almost structureless continuum in the 300–400-Å region.

The Ba^{2+} absorption spectrum was recorded by integrating 300 pulses photographically on a 3-m grazing-incidence spectrograph with a resolution of 0.05 Å (~ 40 cm^{-1}). The low members of the Ba^{2+} Rydberg series, which were measured accurately by Hellentin,[6] the second-order He absorption lines,[7] and the few uranium lines[8] arising from the BRV anode were used as wavelength standards. These lines unfortunately appear only near the ends of the spectral region of interest. We therefore used the grating equation, modified by a quadratic term adjusted to give a better fit to the standard lines, to determine the Ba^{2+} wavelengths. We estimate that the resulting wavelength uncertainty is about ± 0.03 Å (± 25 cm^{-1}).

III. ANALYSIS OF THE SPECTRUM

The photoabsorption spectrum shown in Fig. 1 can be classified in terms of five interacting Rydberg series conveniently labeled by the J-j coupling notation $^2P_{3/2}ns_{1/2}$, $^2P_{3/2}nd_{3/2}$, $^2P_{3/2}nd_{5/2}$, $^2P_{1/2}ns_{1/2}$, and $^2P_{1/2}nd_{3/2}$ (all with $J=1$). In this paper each of these series will be referred to as a "channel" and denoted by the abbreviations ns, $n\bar{d}$, nd, ns', and nd', respectively. The first three channels describe three discrete (or bound) Rydberg series converging to the $5p^5\,{}^2P_{3/2}$ (or I_1) limit. The fourth and fifth channels describe two series converging to the second limit, $5p^5\,{}^2P_{1/2}$ (or I_2). The members of the latter two series which lie above I_1 (i.e., when $n \geq 10$ for the nd series and when $n \geq 11$ for the ns series) are degenerate with the continuum states of the first three channels.

Because the channel interaction was relatively weak, we were able to use Rydberg-Ritz formulas for these series with quantum defects derived from the lower series members, reported by Hellentin, to identify the higher members present in our spectrum. These identifications are given in Table I along with wavelengths and quantum defects relative to I_1 and I_2. Values for I_1 and I_2 were also taken from Hellentin's analysis of the Ba^{2+} and Ba^{3+} emission spectra.[6] We found that nearly exact coincidence of $n\bar{d}$ and $(n+1)s$ resonances for $n \geq 9$ was predicted from the Rydberg-Ritz formulas, a fact which was confirmed by the RRPA calculation. These resonances are given ns assignments in Fig. 1 and Table I, because the RRPA calculation shows that the ns resonances are much stronger than the coincident $n\bar{d}$ resonances, except for $12\bar{d}$ and $19\bar{d}$ which are calculated to be of comparable strength to the $13s$ and $20s$ resonances.

Table II summarizes the results of our *ab initio* RRPA calculation in which the eigenquantum defects and eigendipole amplitudes were obtained for each bound resonance. The actual physical eigenenergies and eigenvector components of each bound state were derived from the eigenquantum defects by solving a set of algebraic equations as determined by the boundary conditions, and absorption oscillator strengths (gf) were deduced from the eigendipole amplitudes.[3] To account for relaxation effects, the theoretical I_1 threshold was lined up with the experimental one; the required shift was less than 10 eV

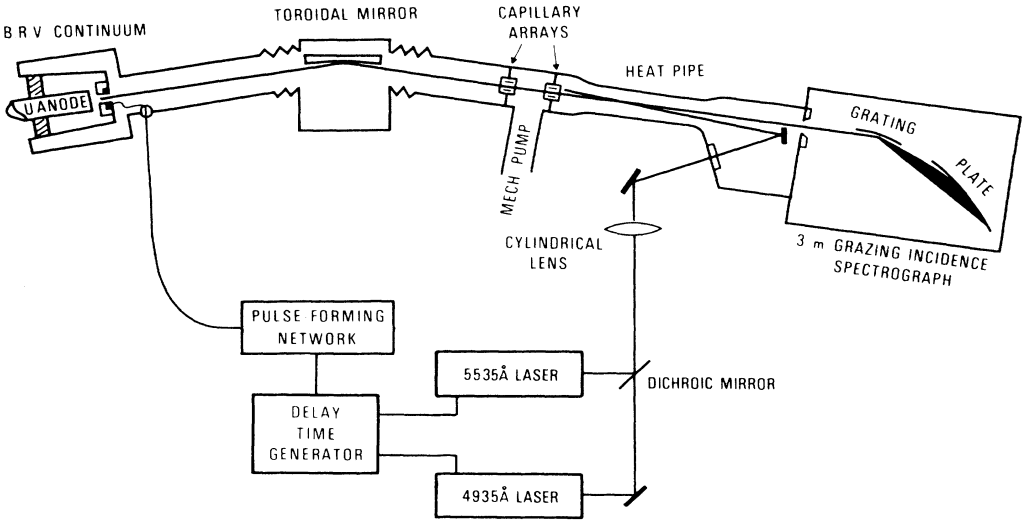

FIG. 2. Experimental apparatus.

TABLE I. Classifications of Ba^{2+} resonances. First threshold is at 345.90 Å.

Wavelength (Å)	Wave number (10^{-5} cm^{-1})	Designation[b]	ν_1[c]	ν_2[c]
423.843[a]	2.359 36	$7s'(\frac{1}{2},\frac{1}{2})$	4.3103	3.7373
420.119[a]	2.380 28	$6d'(\frac{1}{2},\frac{3}{2})$	4.3975	3.7937
407.118[a]	2.456 29	$8s(\frac{3}{2},\frac{1}{2})$	4.7665	4.0231
403.821[a]	2.476 34	$7d(\frac{3}{2},\frac{5}{2})$	4.8804	4.0909
386.19	2.5894		5.7224	4.5498
385.40	2.5947	$9s(\frac{3}{2},\frac{1}{2})$	5.7734	4.5755
384.16	2.6031		5.8571	4.6166
384.04	2.6039	$8d(\frac{3}{2},\frac{5}{2})$	5.8649	4.6204
380.29	2.6296	$8s'(\frac{1}{2},\frac{1}{2})$	6.1468	4.7545
378.60	2.6413	$7d'(\frac{1}{2},\frac{3}{2})$	6.2895	4.8197
377.53	2.6488		6.3858	4.8626
373.73b1	2.6757		6.7738	5.0275
373.67b1	2.6762	$10s(\frac{3}{2},\frac{1}{2})$	6.7804	5.0302
372.78	2.6825	$9d(\frac{3}{2},\frac{5}{2})$	6.8838	5.0720
366.87	2.7257		7.7306	5.3836
366.79	2.7264		7.7456	5.3887
366.58	2.7279	$11s(\frac{3}{2},\frac{1}{2})$	7.7815	5.4007
366.06	2.7318	$10d(\frac{3}{2},\frac{5}{2})$	7.8767	5.4322
361.93	2.7630	$12s(\frac{3}{2},\frac{1}{2})$	8.7824	5.7041
361.63	2.7652	$11d(\frac{3}{2},\frac{5}{2})$	8.8621	5.7257
361.12	2.7692	$9s'(\frac{1}{2},\frac{1}{2})$	9.0024	5.7631
360.25	2.7758	$8d'(\frac{1}{2},\frac{3}{3})$	9.2607	5.8291
358.69	2.7879	$13s(\frac{3}{2},\frac{1}{2})$	9.7878	5.9541
358.42	2.7901	$12d(\frac{3}{2},\frac{5}{2})$	9.8915	5.9772
356.36	2.8061	$14s(\frac{3}{2},\frac{1}{2})$	10.7883	6.1590
356.18	2.8076	$13d(\frac{3}{2},\frac{5}{2})$	10.8827	6.1764
354.62	2.8199	$15s(\frac{3}{2},\frac{1}{2})$	11.7889	6.3290
354.48	2.8211	$14d(\frac{3}{2},\frac{5}{2})$	11.8830	6.3434
353.28	2.8306	$16s(\frac{3}{2},\frac{1}{2})$	12.7898	6.4708
353.18	2.8314	$15d(\frac{3}{2},\frac{5}{2})$	12.8769	6.4820
352.23	2.8391	$17s(\frac{3}{2},\frac{1}{2})$	13.7897	6.5897
352.15	2.8397	$16d(\frac{3}{2},\frac{5}{2})$	13.8756	6.5990
351.39	2.8458	$18s(\frac{3}{2},\frac{1}{2})$	14.7898	6.6903
351.34	2.8463	$17d(\frac{3}{2},\frac{5}{2})$	14.8620	6.6969
350.77	2.8509	$10s'(\frac{1}{2},\frac{1}{2})$	15.6880	6.7677
350.70b1	2.8514	$19s,(\frac{3}{2},\frac{1}{2})$	15.8004	6.7767
350.29	2.8547	$9d'(\frac{1}{2},\frac{3}{2})$	16.5040	6.8293
350.14b1	2.8599	$20s,19d$	16.7964	6.8497
350.08b1	2.8565	$19d(\frac{3}{2},\frac{5}{2})$	16.9101	6.8572
349.65b1	2.8600	$21s,20d$	17.8499	6.9158
349.27b1	2.8631	$22s,21d$	18.8278	6.9689
348.91b1	2.8660	$23s,22d$	19.8967	7.0193
344.48	2.9029	$11s'(\frac{1}{2},\frac{1}{2})$		7.7707
344.16	2.9056	$10d'(\frac{1}{2},\frac{3}{2})$		7.8352
340.35	2.9381	$12s'(\frac{1}{2},\frac{1}{2})$		8.7712
340.14	2.9400	$11d'(\frac{1}{2},\frac{3}{2})$		8.8358
337.51	2.9629	$13s'(\frac{1}{2},\frac{1}{2})$		9.7634
337.34	2.9643	$12d'(\frac{1}{2},\frac{3}{2})$		9.8324
335.41	2.9814	$14s'(\frac{1}{2},\frac{1}{2})$		10.7757
335.32	2.9822	$13d'(\frac{1}{2},\frac{3}{2})$		10.8261
333.90	2.9949	$15s'(\frac{1}{2},\frac{1}{2})$		11.7461
333.80	2.9958	$14d'(\frac{1}{2},\frac{3}{2})$		11.8217
332.65b1	3.0062	$16s',15d$		12.7896
331.72b1	3.0146	$17s',16d'$		13.7977

TABLE I. (*Continued.*)

[a]Wavelength from Hellentin level values (see Ref. 5).
[b]Major eigenvector component. All $n\bar{d}$ above $n=8$ are unresolved from $(n+1)s$ resonances and are much weaker, according to theory (see text and Table II).
[c]Based on $I_1 = 289\,100(20)$ cm^{-1} and $I_2 = 306\,650$ cm^{-1}.

which is a typical offset when comparing experimental binding energies to differences in total energies as calculated in a central-field approximation. The columns in Table II contain the following data: (1) measured wavelengths of absorption lines, (2) observed minus calculated wavelengths, (3) classification of upper state, (4) calculated gf value times 10^4, and (5–9) squared eigenvector components of upper level in J-j coupling.

Table II shows that differences in energy between theory and experiment are less than 1 Å (<0.5)% and that theory tends to underestimate the excitation energies. Although there is substantial mixing between channels, the mixing between the two s channels and between the s and d channels is small. The largest mixing of the s and d channels (<10%) is between the $n\bar{d}$ and ns series, which are nearly degenerate. In addition, when members of the nd and ns series come close to the nd' and ns' resonances, significant mixing or configuration interaction is observed. Some examples seen in Table II are the $12d$, $18d$, and $19d$, the $19s$ and $18\bar{d}$; this feature of configuration or channel interaction will be shown also in the graphical analysis of Fig. 3 described below.

In Figs. 3(a), 3(b), and 3(c), we have plotted the experimental photoabsorption spectrum as a function of ν_2, the Lu-Fano plot[2] (ν_1 [mod 1] versus ν_2), and the calculated relative absorption strengths. The Lu-Fano plot was generated in a semiempirical manner. The curve was determined by the experimental points, except in the regions of interaction where there was insufficient data. In these regions, the shapes of the curves were determined by the energy-dependent MQDT parameters of the RRPA technique.[3] In this way we obtained a Lu-Fano plot consistent with the observations, but with details in the complicated curve anticrossing region determined by theory. (There are not enough experimental data to fully determine this complicated region empirically.)

As is well known, for two-limit systems in the approximation where channel interactions are weak, the Lu-Fano plot will consist of a set of horizontal lines (for the series going to the first limit, constant ν_1 [mod 1]) and vertical lines (for the series going to the second limit, constant ν_2 [mod 1]) with sharp, closely spaced avoided crossings preventing intersections of the lines. These curves are the quantum-defect functions, which are analytic continuations of the phase shifts [mod π] from the continuum.[2]

In Ref. 1, the spectrum of Ba^{2+} was compared to that of the isoelectronic Cs^+ and Xe to show how increasing the nuclear charge affects the interchannel interactions. As the interchannel interaction increases, the widths of the avoided crossings between interacting channels increase and the curves increasingly deviate from the limiting case of two vertical and three horizontal lines. Figure 2 of Ref. 1 shows clearly the enhancement of interchannel interaction between the three d channels as one progresses from Ba^{2+} (small interchannel interactions) to Cs^+ and to Xe (strong interchannel interactions). The same figure shows the corresponding increase in nd' autoionization width with increasing channel interaction, an increase of about 50% from Ba^{2+} to Xe.

Channel interaction alters the oscillator-strength distribution below the I_1 threshold as well. At a first glance of Fig. 3(a), one sees an obvious ν_2 periodic intensity enhancement in the ns, nd, and $n\bar{d}$ photoabsorption spectrum corresponding to the cases where members of those series fall near vertical s' and d' branches of the plot. The vertical branches determine the positions of the ns' and nd' levels below I_1 and the shapes and positions of the resonances above I_1. According to MQDT, the oscillator-strength distribution (df/dE) in each period of ν_2 is the same, to first order, both below and above threshold. Thus we can expect that the strength of the bound ns, nd, and $n\bar{d}$ resonances will be altered whenever they happen to fall in the vicinity of the near vertical s' and d' branches. Specifically, this alteration will occur when these resonances fall within a distance of the vertical branches roughly given by the extent of the avoided crossing in ν_2 space, which in turn, corresponds to the widths of the autoionizing resonances ns' or nd' above I_1.

In the absence of channel interaction, the oscillator strengths of a Rydberg series should decrease smoothly with increasing n as $1/n^{*3}$, where n^* ($=\nu_{1,2}$) is the appropriate effective quantum number of the nth level. Figure 3(c) displays the channel interaction contained in the calculations represented in Table II in a graphic way. The bar graph represents the gf values (column 3) for a selected group of bound resonances located by the "lines" at the appropriate ν_2. The nd series shows the effects of the interaction most clearly, and for this series we have indicated with a dot on the line representing the gf value the relative value to be expected if the normal $1/n^{*3}$ rule prevailed. The largest enhancements in intensity are seen to occur at $7d$, $9d$, and $12d$ when these bound resonances are near the end of the rising nd' branches. As mentioned earlier, the $18d$, $19d$, $19s$, and $18\bar{d}$ also manifest largest interchannel interactions which show up in Table II; the line at $\nu_2 \approx 6.8$ corresponding to the blended $10s', 19s$ resonances obviously has an anomalously large valve.

To compare the calculated data with the actual photoabsorption spectrum of Fig. 3, we must take into account the following experimental factors.

(1) The spectrum was obtained on photographic plates which have both a nonlinear response and a nonuniform sensitivity, varying with position on the plate.

(2) The Ba^{2+} ions were embedded in a fairly dense plasma which significantly broadened the higher n levels.

The first factor is probably responsible for the apparent decrease in line strength seen for ν_2 between 4 and 5 ($\lambda \sim 380$ Å). In this region of the plate, there was significant background (which was numerically reduced) due to the second-order transmission through the He buffer gas near the He resonances at 206 and 194 Å:[7] this caused near saturation densities on the plate. Thus the $7d$ absorption appears smaller than the $8d$ in spite of the larger calculated gf value.

The second factor broadens the levels to a width which

TABLE II. Calculated weighted oscillator strength (gf) of absorption lines of Ba^{2+} below threshold, and squared eigenvector components of upper level. The calculated wavelengths are compared with the observed under "differ". A dash means a very small value but not necessarily zero.

	Wavelength (Å)				% composition of upper level squared			
				$\bar{d}$	d	d'	s	s'
nl	Obs.	Diff.	$10^4 gf$	$(\frac{3}{2},\frac{3}{2})$	$(\frac{3}{2},\frac{5}{2})$	$(\frac{1}{2},\frac{3}{2})$	$(\frac{3}{2},\frac{1}{2})$	$(\frac{1}{2},\frac{1}{2})$
$8s$	407.118[a]	1.01	655	7.3	0.8	0.2	91.2	0.5
$9s$	385.40	0.47	219	1.0	0.2		98.7	0.1
$10s$	373.67	0.26	162	6.2	1.2	0.2	91.9	0.4
$11s$	366.58	0.17	91	1.7	0.4		97.8	
$12s$	361.93	0.11	48	0.2			98.2	1.6
$13s$	358.69	0.07	38	1.9	0.2	0.6	96.5	0.8
$14s$	356.36	0.05	36	7.2	1.6	0.1	90.8	0.2
$15s$	354.62	0.04	25	1.7	0.4		97.8	0.1
$16s$	353.28	0.03	18	0.5	0.1		99.4	
$17s$	352.23	0.03	14	0.1			99.9	
$18s$	351.39	0.02	10				99.2	0.8
$19s$	350.70	0.01	3	4.9	2.7	1.2	70.3	20.8
$20s$	350.14b1	.01	11	0.1	0.2	0.1	93.7	5.8
$7\bar{d}$	407.559[a]	0.76	2	72.0	14.0	6.4	7.6	
$8\bar{d}$	386.19	1.03	3	74.3	24.2	0.3	1.2	
$9\bar{d}$	373.73	0.31	4	73.0	14.6	5.2	7.2	
$10\bar{d}$	366.58[b]	0.12	1	76.3	21.4	0.2	2.1	
$11\bar{d}$	361.93[b]	0.06		69.9	26.3	3.3	0.2	0.2
$12\bar{d}$	358.69[b]	0.09	19	74.4	10.4	13.0	2.0	0.2
$13\bar{d}$	356.36[b]	0.05		72.3	17.1	1.8	8.8	
$14\bar{d}$	354.58[b]	0.04		76.8	20.6	0.4	2.1	
$15\bar{d}$	353.28[b]	0.03		77.0	22.4		0.6	
$16\bar{d}$	352.23[b]	0.02		75.6	24.0	0.3	0.1	
$17\bar{d}$	351.39[b]	0.02		71.8	25.8	2.2		0.2
$18\bar{d}$	350.70[b]	0.00		46.1	20.8	10.0	6.4	16.7
$19\bar{d}$	350.14b1[b]	−0.02	12	9.0	11.5	78.8	0.1	0.6
$7d$	403.819[a]	1.11	2170	16.9	78.9	4.2		
$8d$	384.04	0.70	542	25.8	73.1	1.0		
$9d$	372.78	0.50	505	17.2	78.9	3.9		
$10d$	366.06	0.26	226	22.2	77.7	0.1		
$11d$	361.63	0.19	90	27.8	67.9	4.2		
$12d$	358.42	0.13	174	12.4	75.2	12.4		
$13d$	356.18	0.10	88	19.1	79.3	1.6		
$14d$	354.48	0.07	59	21.2	78.5	0.3		
$15d$	353.18	0.06	41	22.7	77.3			
$16d$	352.15	0.05	29	24.2	75.5	0.2		
$17d$	351.34	0.05	20	26.4	71.9	1.7		
$18d$	(350.63)[c]		12	29.6	61.6	8.2		0.4
$19d$	350.08b1	−0.01		36.5	18.7	44.8		
$8s'$	380.29	0.87	192			0.2	0.2	99.6
$9s'$	361.12	0.48	112	0.1			0.3	99.6
$10s'$	350.77	0.22	64	0.1			0.5	99.3
$7d'$	378.60	0.80	781		0.7	99.0		0.3
$8d'$	360.25	0.51	331		0.2	99.8		
$9d'$	350.29	0.37	157	0.1	2.0	97.9		

[a]Wavelength from Hellentin level values (see Ref. 6).

[b]Unresolved from ns levels.

[c]Calculated wavelength. This level was not observed (see text).

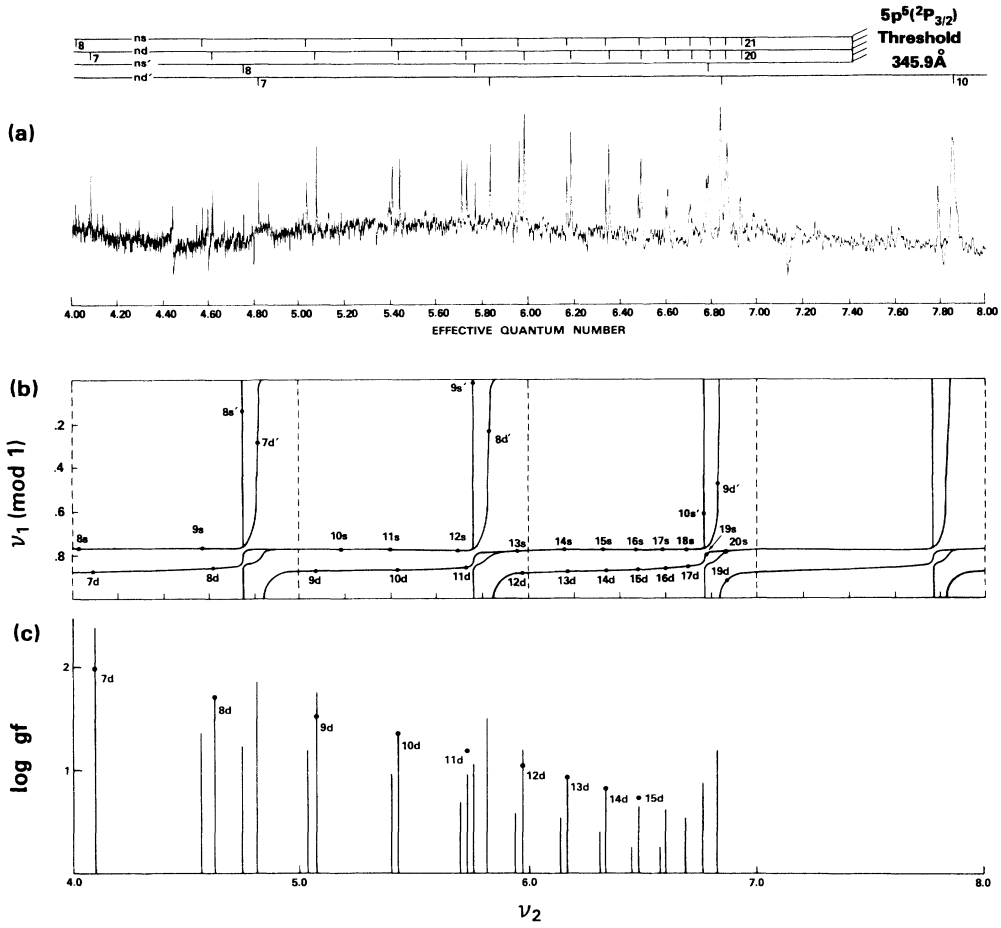

FIG. 3. (a) Photographic spectrum plotted as a function of ν_2. (b) Lu-Fano plot constructed from theoretical model with displacement of ν_2 to align experimental and theoretical energy values. (c) Bar graph of calculated gf values. Length of line represents value calculated by RRPA method and dot on nd series members is the $1/n^{*3}$ value normalized to the $8d$ theoretical value.

increases as n^{*2}. This broadening was observed in an earlier similar experiment in which a Cs^+ spectrum was taken with a high-resolution 10.7-m grazing-incident spectrograph;[9] there, for example, broadening was clearly observed beyond the instrumental limit for the nd levels for $n \geq 11$. The broadening increases the equivalent width of the absorption line, and since most of the lines we observe have instrumentally limited widths, this increases the height of the line. Lack of knowledge about the line-broadening parameters for Ba^{2+} and the exact conditions of the plasma prevent an accurate calculation of the broadening, but an estimate shows it to be a significant factor for all $n^* \geq 6.8$. Consequently, we believe that the plasma broadening accounts for a large fraction of the discrepancy between the calculated and observed strengths for the higher series members. In particular, the fact that the observed magnitudes of the nd lines for $n=9,12$ are larger than the neighboring $n'd'$ lines (for $n'=7,8$, respectively) or that the $7d'$, $8d'$, and $9d'$ lines are in order of ascending magnitude rather than vice versa as predicted by theory can probably be attributed to the n^{*2}-dependent increase in equivalent width.

The region near the $9d'$ and $10s'$ vertical branches ($\nu_2 \approx 6.8$) provides the most notable example of interchannel mixing. The spectrum displays a significant enhancement in the oscillator strength for the blended lines near the $9d'$ and $10s'$, the envelope of which resembles the shape of the autoionizing profiles. Since df/dE below I_1 is approximately the same as that above I_1, the fact that it has a minimum for ν_2 [mod 1] ~ 0.79 above I_1 explains why the $18d$ resonance, predicted to have a value for $\nu_2=6.7881$ ($\lambda=350.63$), is absent from our spectrum. This variation in df/dE is quite sharp; notice that the $10s'$ at $\nu_2=6.7677$ and the $19s$ at 6.7767, which are barely resolved, do have significant oscillator strength.

Although the calculated df/dE reproduces the general features observed quite well, the associated gf values for individual levels are not as accurate in the region of $\nu_2=6.8$ because the calculation here is extremely sensitive to small changes in the eigenenergies. As stated earlier, the theoretical energy levels tended to be lower than the experimental values. Thus, whereas the $19d$ is predicted to fall near the theoretical minimum and in consequently calculated to have very little oscillator strength (see Table II), it is the $18d$ which falls near the true minimum and hence is absent from our spectrum.

ACKNOWLEDGMENTS

The authors would like to thank C. W. Clark, C. Cromer, M. Ginter, W. Johnson, and T. J. McIlrath for helpful discussions. Partial support from the U.S. Air Force Office of Scientific Research under Contract No. ISSA 86-0023 and the National Science Foundation under Grant No. PHY-84 51284 is gratefully appreciated.

[1]W. T. Hill, III, K. T. Cheng, W. R. Johnson, T. B. Lucatorto, T. J. McIlrath, and J. Sugar, Phys. Rev. Lett. **49**, 1631 (1982).
[2]U. Fano, Phys. Rev. A **2**, 353 (1970); K. T. Lu, *ibid.* **4**, 579 (1971); C.-M. Lee and K. T. Lu, *ibid.* **8**, 1241 (1973).
[3]W. R. Johnson, K. T. Cheng, K.-N. Huang, and M. Le Dourneuf, Phys. Rev. A **22**, 989 (1980).
[4]T. B. Lucatorto and T. J. McIlrath, Appl. Opt. **19**, 3948 (1980).
[5]T. B. Lucatorto, T. J. McIlrath, and G. Mehlman, Appl. Opt. **18**, 2916 (1979).
[6]P. Hellentin, Phys. Sci. **13**, 155 (1976).
[7]R. P. Madden and K. Codling, Phys. Rev. Lett. **10**, 516 (1963).
[8]G. H. Newsom, Appl. Opt. **13**, 2712 (1974).
[9]T. J. McIlrath, J. Sugar, V. Kaufman, D. Cooper, and W. T. Hill III, J. Opt. Soc. Am. B **3**, 398 (1986).